Article | Open Access

Energy Materials

Zhang *et al. Energy Mater.* **2026**, *6*, 600161 **DOI:**10.20517/energymater.2026.295

# Precursor aging homogenizes $PbI_2$ sol-clusters for humidity-tolerant fabrication of perovskite solar cells

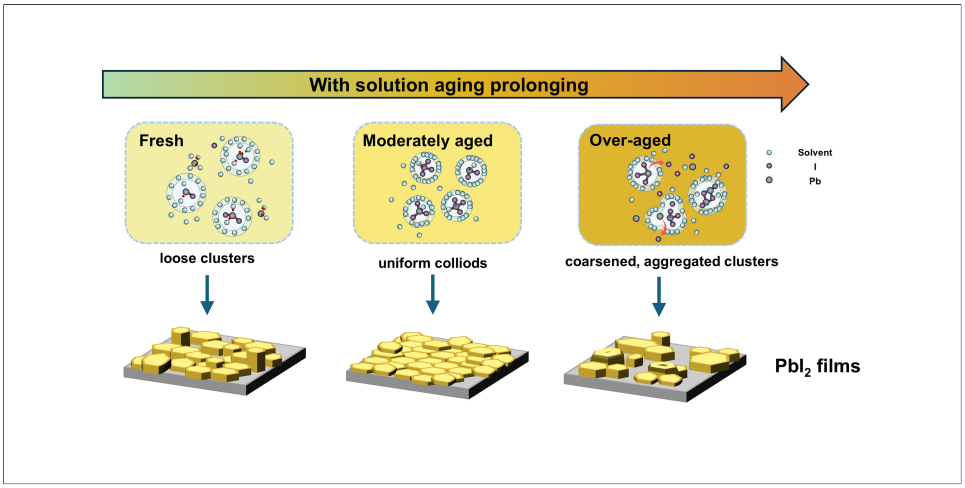
**Mingjun Zhang[1], Qiang Zeng[1,2,3,*], Xiang Liao[1,2], Kexin Mi[1,2], Linhong Li[1,3], Wentong Yang[1,3], Fangyang Liu[1,2,3,*]**

**Keywords:**
Perovskite solar cells, $PbI_2$ precursor, solution aging, humidity-tolerant fabrication

**Citation:** Zhang, M.; Zeng, Q.; Liao, X.; Mi, K.; Li, L.; Yang, W.; Liu, F. Precursor aging homogenizes $PbI_2$ sol-clusters for humidity-tolerant fabrication of perovskite solar cells. *Energy Mater.* **2026**, *6*, 600161. https://dx.doi.org/10.20517/energymater.2026.295

**Received:** 30 Aug 2026 **First Decision:** 23 Sep 2026 **Revised:** 27 Oct 2026 **Accepted:** 5 Nov 2026 **Published:** 20 Nov 2026

**Academic Editor:** Federico Bella
**Copy Editor:** Ping Zhang
**Production Editor:** Ping Zhang




## Abstract

Hybrid organic-inorganic metal halide perovskite solar cells (PSCs) represent a promising next-generation photovoltaic technology. Two-step sequential deposition is widely used for the scalable ambient-condition fabrication of perovskite films because of its high processing tolerance and reproducibility, with the predeposited lead iodide ($PbI_2$) layer acting as a vital scaffold for perovskite crystallization and largely determining the final device performance. Despite extensive progress in $PbI_2$ layer regulation through additive and solvent engineering, the physicochemical evolution of precursor systems during the early stages of aging (prior to apparent deterioration) is insufficiently understood. Herein, we investigate the effects of early-stage $PbI_2$ precursor aging on the growth of perovskite films and device performance via ambient two-step deposition. We identify a moderate-aging processing window, in which the spontaneous evolution of the $PbI_2$ solution yields a desirable physicochemical state for the subsequent thin-film deposition. The PSCs fabricated using an additive-free precursor solution at a relative humidity of 40%-50%

Check for updates

[1]School of Metallurgy and Environment, Central South University, Changsha 410083, Hunan, China.
[2]Engineering Research Centre of Advanced Battery Materials, Ministry of Education, Central South University, Changsha 410083, Hunan, China.
[3]National Engineering Research Center of Low-carbon Nonferrous Metallurgy, Central South University, Changsha 410083, Hunan, China.

***Correspondence to:** Prof. Qiang Zeng, Prof. Fangyang Liu, School of Metallurgy and Environment, Central South University, Changsha 410083, Hunan, China; Engineering Research Centre of Advanced Battery Materials, Ministry of Education, Central South University, Changsha 410083, Hunan, China; National Engineering Research Center of Low-carbon Nonferrous Metallurgy, Central South University, Changsha 410083, Hunan, China. E-mail: qiang.zeng@csu.edu.cn; liufangyang@csu.edu.cn

exhibit a power conversion efficiency (PCE) of 24.52%. This work elucidates the positive role of controlled precursor aging, enriches existing $PbI_2$ modulation strategies, and provides a facile, low-cost approach to high-efficiency all-air-processed PSCs.

## INTRODUCTION

Hybrid organic-inorganic metal halide perovskite solar cells (PSCs) have garnered considerable attention due to their exceptional optoelectronic properties[1-4]. Over the past decade, PSCs have achieved a power conversion efficiency (PCE) exceeding 27%, positioning them as promising candidates for next-generation photovoltaic technology[5]. Air-processed PSCs are highly desirable for scalable, cost-effective manufacturing. Compared with one-step methods, two-step sequential deposition methods offer the benefits of a broader processing window and higher reproducibility and are therefore more widely used[6-8]. The lead iodide ($PbI_2$) layer serves as a structural scaffold for subsequent perovskite crystallization, which is initiated by the infiltration of organic ammonium salts into the predeposited lead halide framework. However, incomplete phase transformation and moisture-induced erosion result in excess residual $PbI_2$, which accelerates charge recombination and structural degradation[9-12]. Therefore, $PbI_2$ film optimization is crucial for methods involving two-step sequential deposition in ambient air.

Considerable effort has been devoted to regulating $PbI_2$ film formation via additive and solvent engineering[13-16]. These strategies can modulate crystallization kinetics during deposition, coordination environments, and intermediate-phase formation, thereby dictating the morphology and reactivity of the resulting $PbI_2$ layers[10,17-19], but rely on externally introduced molecular species. Beyond external regulation, the intrinsic evolution of precursor solution chemistry can also play an important role in subsequent film formation, as even slight changes in precursor chemistry can be amplified during the formation of the $PbI_2$ template and its conversion into perovskite in two-step deposition. Solution aging is a spontaneous evolution process continuously influencing the physicochemical state of precursor systems. Prolonged aging can induce changes in solute coordination[20-23], colloidal aggregation[21,24,25], and halide speciation[26-29] and is therefore often associated with deteriorated film morphology and degraded device performance. In particular, colloidal aggregation and the oxidation of iodide ions ($I^-$) have been regarded as major contributors to precursor degradation during long-term storage. To mitigate these effects, stabilizers have been widely employed to extend the shelf life of precursor solutions. Although the above-mentioned studies provide important insights into the detrimental consequences of prolonged aging, the physicochemical evolution of precursor systems in the early stages of aging, prior to apparent deterioration, remains insufficiently understood.

In this work, a sequential deposition approach was used to systematically investigate the effects of the early-stage aging of $PbI_2$ precursor solutions on the formation of perovskite films and the photovoltaic performance of devices. Our findings reveal a moderate-aging processing window wherein the intrinsic evolution of the $PbI_2$ solution leads to a physicochemical state favoring subsequent film deposition, whereas over-aging disrupts this equilibrium. Specifically, moderate aging (5 days) improved the uniformity of $PbI_2$ films and enhanced perovskite crystallization quality. Devices fabricated from the moderately aged $PbI_2$ solution exhibited enhanced PCE of 24.52% under 40%-50% relative humidity (RH) without any additives. This study clarifies the role of controlled precursor aging during sequential deposition in the regulation of $PbI_2$-based systems, showing that controlled early-stage aging offers a simple and practical way to enhance all air-processed perovskite solar cells without using extra chemical additives or complicated processing methods.

## EXPERIMENTAL

### Materials

All chemicals and reagents used in this study were used without further purification. $SnO_2$ colloidal solution (15 wt% in water) was purchased from Alfa Aesar. N,N-Dimethylformamide (DMF, 99.8%), Dimethyl sulfoxide (DMSO, 99.9%), isopropanol (IPA), chlorobenzene (CB), acetonitrile (ACN), 4-tert-butylpyridine (t-BP), and lithium bis(trifluoromethanesulfonyl)imide (Li-TFSI) were purchased from Sigma-Aldrich. Lead iodide ($PbI_2$, 99.99%) was purchased from Zhejiang Yitai Technology (China). $NiO_x$ nanoparticle powder (99.999%, particle size around 10 nm) was purchased from Advanced Election Technology Company. Formamidinium iodide (FAI), methylammonium iodide (MAI), methylammonium chloride (MACl), phenylethylamine iodide (PEAI), phenyl-C61-butyric acid methyl ester ($PC_{61}BM$), and 2,2',7,7'-Tetrakis[N,N-di(4-methoxyphenyl)amino]-9,9'-spirobifluorene (Spiro-OMeTAD) (99.8%) were all purchased from Xi'an Yuri Solar (China).

### Device fabrication

#### *n-i-p perovskite solar cell fabrication*

Indium tin oxide (ITO) glass substrates were cleaned via sequential ultrasonication in detergent, deionized water, acetone, and IPA for 15 min each, followed by a 20-min ultraviolet (UV)-ozone treatment. An electron transport layer was then deposited by spin-coating a diluted $SnO_2$ nanoparticle dispersion (3 wt% in deionized water) at 5,000 rpm for 30 s, and the films were annealed at 150 °C for 30 min in ambient air. Prior to perovskite deposition, the $SnO_2$-coated substrates underwent an additional 10-min UV-ozone activation. The perovskite films were prepared using a two-step sequential deposition method under ambient conditions with a RH of 40-50%. A 1.5 M $PbI_2$ precursor solution in DMF:DMSO (9:1 v/v) was prepared and stored in a sealed vial at 25 ± 2 °C under ambient light for the specified aging period, with aging time counted from preparation completion. $PbI_2$ solution was then spin-coated at 2,000 rpm for 30 s, annealed at 70 °C for 20 s, and then cooled to room temperature. Subsequently, an organic salt solution containing 90 mg FAI, 6.39 mg MAI, and 9 mg MACl in 1 mL IPA was deposited at 2,000 rpm for 30 s, and the film was annealed at 150 °C for 15 min to achieve full crystallization. For surface modification, a PEAI solution (5 mg $mL^{-1}$ in IPA) was spin-coated onto the perovskite layer at 5,000 rpm for 20 s without further annealing. The hole transport layer was then deposited at 4,000 rpm for 20 s using a Spiro-OMeTAD solution, which was prepared by mixing 72.3 mg Spiro-OMeTAD, 28.8 μL 4-tert-butylpyridine, and 17.5 μL Li-TFSI solution (520 mg $mL^{-1}$ in acetonitrile) in 1 mL chlorobenzene. Both PEAI and Spiro-OMeTAD layers were processed in ambient air at 40%-50% RH. Finally, a 70-nm-thick Ag electrode was deposited by thermal evaporation in high vacuum.

#### *Single-carrier device fabrication*

Electron-only and hole-only devices were fabricated with the structures of ITO/$SnO_2$/perovskite/$PC_{61}BM$/Ag and ITO/$NiO_x$/perovskite/Spiro-OMeTAD/Ag, respectively. For the electron-only devices, a $PC_{61}BM$ layer was deposited onto the perovskite film by spin-coating at 2,000 rpm for 30 s, followed by thermal evaporation of the Ag electrode. For the hole-only devices, a $NiO_x$ nanoparticle dispersion was spin-coated onto the ITO at 3,000 rpm for 20 s. The $NiO_x$ layer was annealed at 150 °C for 10 min in ambient air before perovskite deposition. The other layers were deposited following the same procedures used in n-i-p perovskite solar cell fabrication.

### Characterization

The chromaticity coordinates of $PbI_2$ precursor solutions were acquired using a Hach LICO 690 high-performance spectral colorimeter. Dynamic light scattering (DLS) measurements on a Malvern Zetasizer Nano ZS90 provided the size distribution of colloids in the $PbI_2$ solutions. Ultraviolet-visible (UV-vis) absorption spectra of both solutions and thin films were collected on a Shimadzu UV-3600i Plus

spectrophotometer in absorbance mode (without integrating sphere), operating at a scan rate of 600 nm/min over 200-450 nm with a step bandwidth of 1 nm. Fourier transform infrared (FTIR) spectra of the $PbI_2$ precursor solutions were recorded with a Thermo Scientific NICOLET iS20 system. $^1$H nuclear magnetic resonance ($^1$H NMR) spectra of the same solutions were measured in DMSO-$d_6$ containing 1% TMS on a Bruker Avance NEO spectrometer running at 600 MHz at room temperature. Free iodide ions ($I^-$) in the $PbI_2$ precursor solutions were quantified via ion chromatography (IC) using a Thermo Scientific ICS-5000+ system. Raman spectra were obtained on a Thermo Scientific DXR3xi Raman spectrometer under 532 nm excitation. Contact angle measurements were performed with a Dataphysics OCA20 system to evaluate the wettability of $PbI_2$ precursor solutions on $SnO_2$ substrates, as well as the hydrophobicity of thin films against water. X-ray diffraction (XRD) patterns were obtained on a PANalytical Empyrean 2 diffractometer with Cu Kα radiation (λ = 1.5405 Å, 40 kV, 100 mA). Top-view and cross-sectional morphologies were examined using a JSM-7610F (JEOL) field-emission scanning electron microscope (SEM) operated at 5 kV. Atomic force microscopy (AFM) was performed on a Bruker Dimension Icon to determine the surface roughness of the thin films. The chemical environment of the perovskite films was analyzed by X-ray photoelectron spectroscopy (XPS) on a ULVAC-PHI VersaProbe 4 system. Photoluminescence (PL) spectra were recorded using an Edinburgh FLS1000 spectrometer. Current density-Voltage (*J-V*) characteristics were measured at 25 °C with a Keithley 2400 source meter under standard Air Mass 1.5 Global (AM 1.5G) illumination (100 mW $cm^{-2}$) provided by a San-Ei Electric solar simulator in ambient air. The light intensity was calibrated against an AK-200 standard silicon solar cell (Konica Minolta). The *J–V* characteristics were recorded in both forward and reverse scan directions over a voltage range of –0.2 to 1.2 V, with a voltage step of 0.02 V and a scan rate of 0.1 V $s^{-1}$. The hysteresis index (HI) was calculated as $(PCE_{reverse} - PCE_{forward})/PCE_{reverse} \times 100\%$, where $PCE_{reverse}$ and $PCE_{forward}$ represent the power conversion efficiencies obtained from the reverse and forward scans, respectively. The steady-state power output (SPO) was monitored under continuous AM 1.5G illumination at the maximum power point. External quantum efficiency (EQE) spectra were collected on a QE-R system (Enlitech), with calibrated Si diodes as references. Capacitance-voltage (*C-V*) and electrochemical impedance spectroscopy (EIS) measurements were both performed using a Keysight E4990A impedance analyzer. The *C-V* measurements were conducted in the dark with a direct current (DC) bias sweeping from -1.0 to 1.5 V and an alternating current (AC) amplitude of 50 mV, while the EIS spectra were recorded under dark short-circuit (DSC) conditions with an AC perturbation amplitude of 30 mV over a frequency range of 2 MHz to 20 Hz. Space-charge-limited current (SCLC) measurements were performed on single-carrier devices in ambient air, with a voltage scanning range from -0.02 to 4 V. The perovskite layer thickness was determined from cross-sectional SEM images of the corresponding n-i-p perovskite solar cells fabricated by the same precursor solution. Specifically, the thickness was measured at the central positions of three representative regions (left, middle, and right), and the average value was used for the calculations. The long-term storage stability of unencapsulated perovskite solar cells was evaluated under ambient air conditions at 25 ± 5 °C and 30 ± 5% RH, with exposure to light avoided. The photovoltaic performance of the devices was periodically monitored throughout the 30-day storage period (720 h).

## RESULTS AND DISCUSSION

To evaluate the effect of early aging on the $PbI_2$ precursor solutions, we first monitored the macroscopic evolution of the solutions over 14 days. We categorized the samples as fresh (1 day), moderately aged (5 days), and over-aged (14 days) for the following study. The yellow $PbI_2$ solutions exhibited progressive color deepening during aging [Figure 1A and B]. The color coordinates shifted near-linearly from (0.42, 0.52) for the fresh sample to (0.44, 0.50) for the over-aged sample, while luminance (Y) concomitantly declined [Supplementary Table 1]. This result indicates that, as aging time increases, the solution gradually changes from light yellow to dark yellow, while its clarity progressively decreases. This progressive color evolution may be associated with changes in the concentration and speciation of iodine-containing species in the

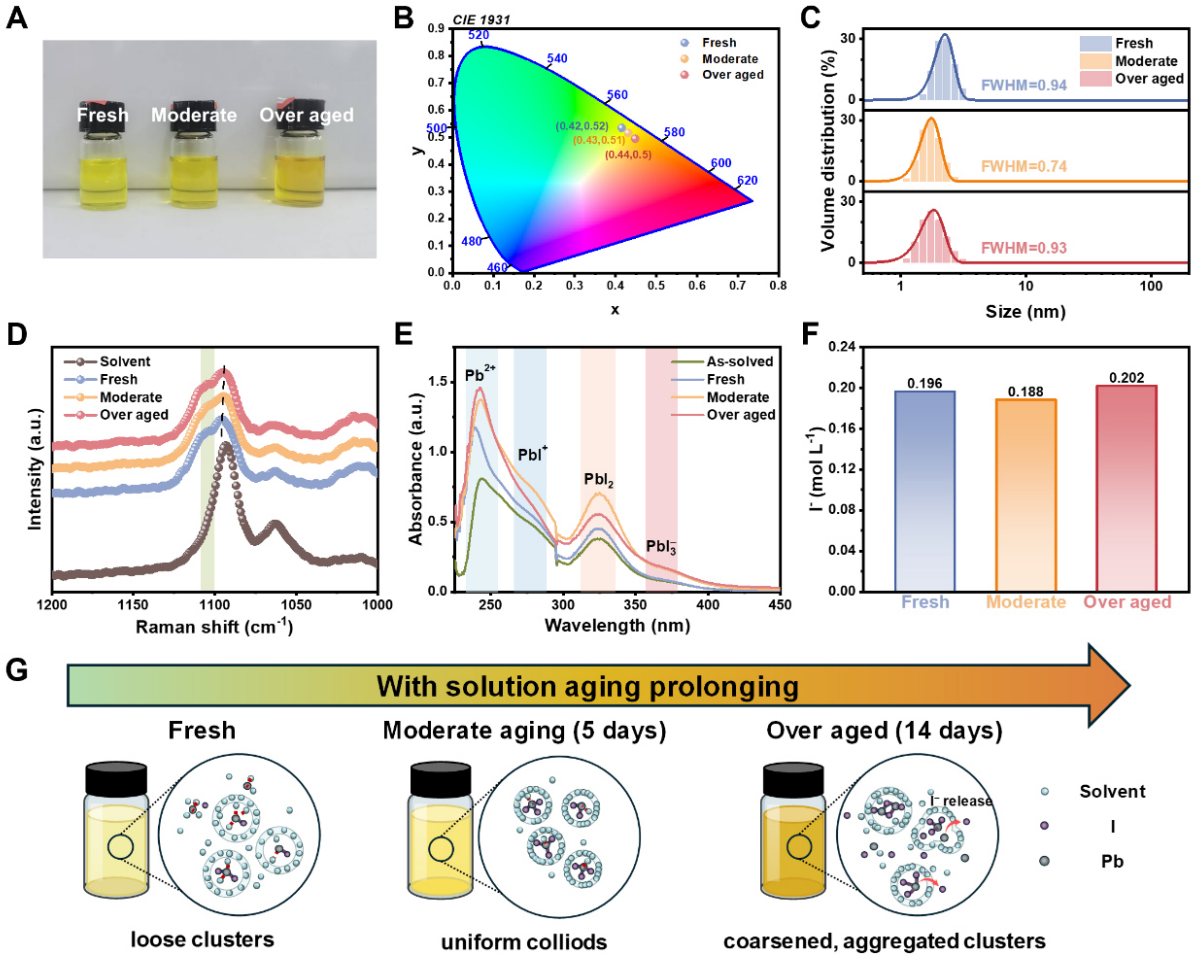



**Figure 1.** Evolution of $PbI_2$ precursor solutions during early aging. (A) The appearance of $PbI_2$ precursor solutions at different aging periods (photographed by the authors); (B) the CIE chromaticity coordinates of $PbI_2$ precursor solutions; (C) the colloid size distribution of $PbI_2$ precursor solutions; (D) Raman spectra; (E) UV-vis absorption; (F) content of free iodide ions in the precursor solutions; (G) Schematic diagram of physical and chemical changes within the solution during early aging. FWHM: Full width at half-maximum; UV-vis: ultraviolet-visible; CIE: Commission Internationale de l'Éclairage.

precursor solution[28].

Given that perovskite precursor solutions form colloidal dispersion systems rather than fully solvated ions[30-32], we used DLS to characterize the particle size distributions of $PbI_2$ precursor solutions. All $PbI_2$ solutions exhibit a predominantly monodisperse distribution with particle sizes of 1-5 nm [Figure 1C] and negligible contributions from larger aggregates (< 0.0005% in volume fraction, Supplementary Figure 1)[32]. The average particle size decreased from ~2.25 nm in the fresh solution to ~1.76 nm after moderate aging, suggesting a more uniform colloidal size distribution. Upon prolonged aging, slight coarsening occurred, with the average size increasing to ~1.85 nm. The predominance of nanoscale colloids in the $PbI_2$ solutions makes light scattering from micrometer-scale aggregates an unlikely explanation for the observed color evolution. To better understand the precursor chemistry, we evaluated the $Pb^{2+}$-solvent interactions by using Raman spectroscopy [Figure 1D]. Upon the dissolution of $PbI_2$, a peak assigned to the rocking vibration of the N-$CH_3$ bond in DMF shifted from 1,093 to 1,096 $cm^{-1}$, with the appearance of a distinct shoulder peak around 1,102 $cm^{-1}$ [Supplementary Figure 2]. This shoulder peak, associated with a more constrained solvent environment, gradually weakened upon aging, which indicated a progressive relaxation of Pb-DMF interactions. This coordination weakening was further confirmed by FTIR spectroscopic analysis [Supplementary Figure 3]. The C=O vibration peak of DMF shifted from 1,667 to 1,635 $cm^{-1}$ upon $PbI_2$ addition and returned to 1,658 $cm^{-1}$ after aging, which suggests the gradual displacement of DMF molecules

from the $Pb^{2+}$ coordination sphere.

UV-vis absorption spectroscopy [Figure 1E] provided further insights into the evolution of iodoplumbate species. The characteristic absorption peaks of $Pb^{2+}$ (~250 nm), $PbI^{+}$ (~270 nm), $PbI_2$ (~325 nm), and $PbI_3^-$ (~370 nm) were identified, consistent with previous reports[33,34]. Upon initial dissolution, the solution exhibited relatively weak absorption, indicating that the coordination equilibrium of Pb-I had not yet been fully established, with low-valent iodoplumbates ($Pb^{2+}$, $PbI^{+}$ and $PbI_2$) constituting the primary species. The raw spectra showed increased absorption features associated with $PbI_2$ and $PbI_3^-$ during moderate aging, followed by a decrease in $PbI^{+}$ and $PbI_2$ and a slight further increase in $Pb^{2+}$ upon over-aging. To further assess these changes, spectral fitting was performed, and the relative contribution of each characteristic absorption feature was calculated from its integrated peak area normalized to the total integrated area of all fitted features. The results are summarized in Supplementary Table 2, with the fitted spectra and relative contribution distributions presented in Supplementary Figure 4. During moderate aging, the proportion of $Pb^{2+}$ contracts from 34.78% to 27.32%, while those of $PbI_2$ and $PbI_3^-$ increase concurrently, rising from 22.25% to 26.71% and from 5.59% to 6.39%, respectively. These changes suggest a redistribution of the iodoplumbates, with an increased relative contribution from the more highly iodinated species ($PbI_2$ and $PbI_3^-$). This trend may be associated with competition between iodide ions and coordinated solvent molecules for $Pb^{2+}$ coordination sites, as discussed in previous studies[33,35]. As aging extends to the over-aged stage, a non-monotonic trajectory emerged: while $PbI_3^-$ showed a slight increase to reach 8.02%, $PbI^{+}$ and $PbI_2$ decreased to 30.83% and 23.64%, respectively. Notably, the $Pb^{2+}$ fraction rebounds to 37.51%, exceeding its level in the moderately aged state, indicating that extended aging induces a secondary reorganization of iodoplumbate species, rather than a continuous shift toward higher iodide coordination. $^1$H NMR spectra show no pronounced chemical shift or new resonances upon aging [Supplementary Figure 5], suggesting that no major changes in the detectable solution-phase chemical species occur during aging. IC measurements captured the dynamic evolution of free $I^-$ concentration during precursor aging [Figure 1F and Supplementary Figure 6]. The $I^-$ concentration declined to 0.188 mol $L^{-1}$ after moderate aging, and then increased to 0.202 mol $L^{-1}$ upon over-aging. The gradual release of $I^-$ during the over-aging stage, accompanied by weakened Pb-solvent interactions, implies a coordination imbalance and partial decomposition within the Pb-I framework.

Figure 1G presents a schematic of the physical and chemical changes in the solution during early aging based on the above results. The early-stage aging of $PbI_2$ precursor solutions can be regarded as a coordination-driven structural refinement process. In the fresh precursor solution, dissolved $PbI_2$ was coordinated by solvent molecules, forming loose agglomerates of colloidal particles. During moderate aging, iodide ions gradually replaced solvent molecules in the $Pb^{2+}$ coordination shell, thereby driving the transformation from low-valent species to high-valent iodoplumbates such as $PbI_3^-$. This chemical rebalancing may be associated with changes in the size distribution and homogeneity of nanoscale colloids, potentially establishing a favorable chemical window for film formation. As shown in Supplementary Figure 7, the contact angle of the precursor on the $SnO_2$ substrate reaches a minimum after moderate aging. This enhanced wettability promoted more uniform precursor spreading, which may have contributed to the uniform nucleation and subsequent growth of high-quality perovskite films. In contrast, over-aging induced the redistribution of Pb-I coordination and $I^-$ release, accompanied by the colloidal coarsening and a shift away from the favorable state. These findings highlight the critical role of controlled early aging in regulating precursor chemistry prior to perovskite film formation. It should be noted that the favorable aging time of 5 days identified in this study is specific to the experimental conditions employed and should not be regarded as universally applicable. Several external factors may alter precursor evolution and shift the favorable aging window. For example, elevated temperature can accelerate iodoplumbate evolution and shorten the time required to reach an optimal precursor state[36], while light exposure can promote the conversion of low-valent to high-valent

iodoplumbate species and induce colloidal aggregation[37,38]. Storage conditions, including sealing and temperature control, may further affect solution composition and colloidal evolution. The key preparation and storage conditions should be controlled to ensure reproducibility.

To further understand the impact of solution aging on film deposition, XRD measurements were performed to analyze the crystallinity of $PbI_2$ films deposited under atmospheric conditions at a RH of 40%-50%. As presented in Figure 2A, the diffraction peaks at 12.69°, 25.55°, and 38.71° correspond to the (001), (002), and (003) lattice planes of $PbI_2$, respectively. Figure 2B provides magnified views of these reflections. The $PbI_2$ film derived from the moderately aged solution displays the most prominent (00n) layered orientation, thus featuring the highest degree of crystallinity, as shown in Supplementary Figure 8. Specifically, while the fresh sample showed a discernible (110) reflection near the (003) peak, this competing orientation was effectively suppressed in the moderately aged film. Over-aging, however, induced a resurgence of the (110) peak intensity and the emergence of the (111) peak. This preferential orientation is quantitatively supported by the diffraction-peak intensity ratios. As depicted in Figure 2C, the (001)/(110) ratio increases from 30.45 for the fresh film to 63.56 for the moderately aged $PbI_2$ film, and sharply decreases to 13.35 upon over-aging. A similar trend was observed for the (003)/(110) ratio [Figure 2D], which was 4.85, 7.95, and 2.31 for the fresh, moderately aged, and over-aged samples, respectively, with the highest ratio observed in the moderately aged sample. Given that the $PbI_2$ (110) plane is oriented perpendicular to the layered (00n) planes, the enhanced (001) peak intensity, together with the decreased (110) peak intensity, suggests a preferential orientation that favors the in-plane growth of the layered $PbI_2$ structure[9,39].

To investigate the impact of solution aging on the morphological characteristics of $PbI_2$, we employed SEM to analyze the surface morphology of $PbI_2$ films [Figure 2E-G]. The fresh film exhibited a relatively uneven surface with discernible hexagonal grain aggregates and sporadic pinholes, whereas the moderately aged $PbI_2$ film presented a compact, homogeneous surface. This morphological refinement is intrinsically linked to the high degree of preferential (00n) orientation revealed by XRD, which facilitates the formation of a dense and continuous precursor template[40]. From a kinetic perspective, a loosely stacked lamellar structure with fewer but larger voids, as observed in the fresh $PbI_2$ film, may partially facilitate the penetration of FAI and MAI solutions[13,41]. However, this morphology often leads to nonuniform reaction kinetics, resulting in incomplete conversion and residual $PbI_2$. In addition, porous $PbI_2$ templates are vulnerable to degradation in ambient air. Moderately aged $PbI_2$ films exhibited grain packing with a high density of smaller and more uniformly distributed voids, which probably served as pathways for solution infiltration and facilitated the subsequent solid-liquid reaction, as reported in previous studies[9,19]. The enhanced wettability of the moderately aged $PbI_2$ film promotes more uniform solution spreading and better interfacial contact compared to the fresh film, which favors the penetration and diffusion of organic cations throughout the compact film. These features enabled a more complete and homogeneous intercalation reaction by improving the diffusion of organic cations into the $PbI_2$ lattice, thus promoting controlled perovskite formation and subsequent crystal growth.

Moreover, the compact $PbI_2$ film obtained after moderate aging exhibited a larger water contact angle, as displayed in Supplementary Figure 9. The reduced surface wettability toward water may help improve its tolerance to ambient moisture under air-processing conditions. By providing a smooth surface with a root mean square (RMS) roughness of 3.09 nm and a highly ordered $PbI_2$ substrate, the moderately aged template could help guide perovskite crystallization and promote structural inheritance in the final film, as supported by XRD data. In contrast, over-aging may lead to a less uniform surface morphology, as reflected by the increased RMS roughness of 4.68 nm compared with 3.25 nm for the fresh sample [Figure 2H-J]. Ultimately, the highly oriented $PbI_2$ crystals in the moderately aged film acted as a structural scaffold that favored uniform nucleation and the controlled growth of subsequent perovskite grains, whereas over-aging may

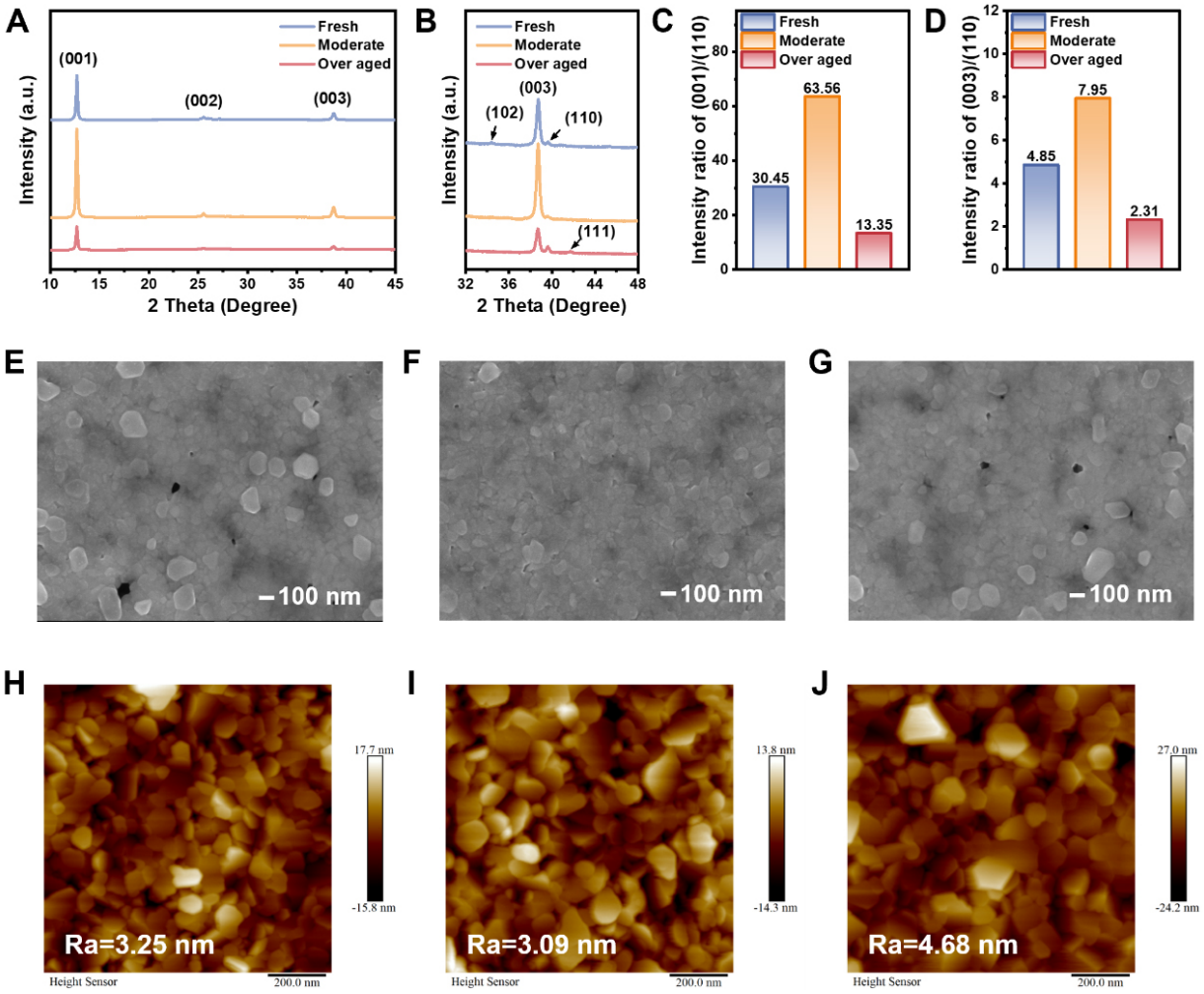



**Figure 2.** Evolution of $PbI_2$ films induced by precursor aging. (A) The XRD patterns of $PbI_2$ films; (B) Magnified XRD patterns in the vicinity of the $PbI_2$ (003) reflection, highlighting the diffraction peaks associated with the (102), (003), (110), and (111) planes; intensity ratios of $PbI_2$ (C) (001)/(110) peak and (D) (003)/(110) peak; surface SEM images of (E) the fresh $PbI_2$, (F) the moderate $PbI_2$ and (G) the over-aged $PbI_2$ films; AFM images of (H) the fresh $PbI_2$, (I) the moderate $PbI_2$ and (J) the over-aged $PbI_2$ films. XRD: X-ray diffraction; AFM: atomic force microscopy; SEM: scanning electron microscope.

drive the system away from the favorable structural window.

Perovskite layers were subsequently fabricated through the intercalation of organic ammonium salts into the $PbI_2$ templates; the crystallinity of the resulting films was further examined by XRD to comprehend the impact of $PbI_2$ solution aging. As depicted in Figure 3A, the marked decrease in the intensity of residual $PbI_2$ peaks upon moderate aging indicates a more complete conversion of the $PbI_2$ precursor. This trend is further supported by the semi-quantitative analysis in Supplementary Figure 10, where the $PbI_2$/(100) intensity ratio decreases from approximately 0.16 for the fresh sample to 0.05 for the moderately aged sample. This decrease corresponds to a substantial reduction in the amount of residual $PbI_2$. Moreover, the perovskite film prepared by the moderately aged solution exhibited stronger (100) and (200) peaks than the fresh film. Compared with the fresh film, the moderately aged sample featured sharper diffraction peaks, with the full width at half-maximum (FWHM) of the (100) and (200) crystal planes reduced from 0.12 and 0.18 to 0.09 and 0.15, respectively, as summarized in Supplementary Table 3. These narrower peaks suggest improved crystalline order, while the enhanced (n00) reflections indicate a more pronounced preferential orientation. Such structural improvements in perovskite films may contribute to more favorable charge transport and reduced charge carrier recombination losses.

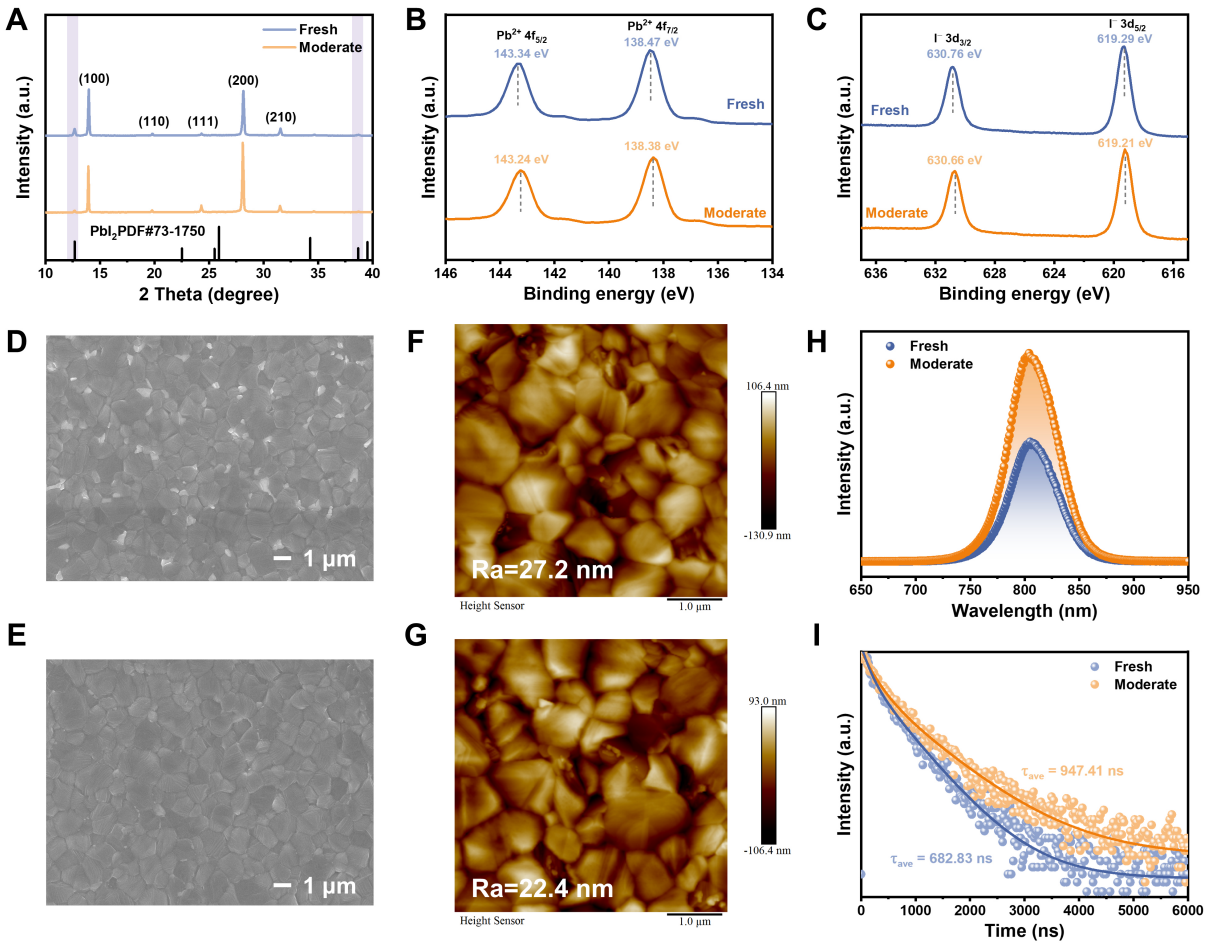



**Figure 3.** Effect of moderate aging on perovskite thin films. (A) The XRD patterns for the fresh and moderately aged perovskite films; the XPS spectra of (B) Pb 4f and (C) I 3d for the fresh and moderately aged perovskite films; surface SEM images of (D) the fresh and (E) the moderately aged perovskite films; AFM images of (F) the fresh and (G) the moderately aged perovskite films; (H) the PL spectra of the fresh and moderately aged perovskite films; (I) the TRPL spectra of the fresh and moderately aged perovskite films. XRD: X-ray diffraction; XPS: X-ray photoelectron spectroscopy; AFM: atomic force microscopy; PL: photoluminescence; TRPL: time-resolved photoluminescence; SEM: scanning electron microscope.

Chemical interactions on perovskite film surfaces were probed by XPS analysis, with the corresponding Pb 4f core-level spectra shown in Figure 3B. The peaks at ~143.34 eV and ~138.47 eV were assigned to the Pb $4f_{5/2}$ and Pb $4f_{7/2}$ components of divalent $Pb^{2+}$ in the fresh sample, respectively, while the perovskite film derived from the moderately aged precursor exhibited a shift of both $Pb^{2+}$-related peaks toward lower binding energies by approximately 0.10 eV. The corresponding I 3d spectra [Figure 3C] displayed characteristic doublets at ~630.76 eV and ~619.29 eV in the fresh perovskite film, which were assigned to the $I^-$ $3d_{3/2}$ and $I^-$ $3d_{5/2}$ components, respectively. Compared with the fresh film, the moderately aged one showed a slight shift of the I 3d peaks to lower binding energies (~0.10 eV). These results suggest a more stabilized Pb-I coordination environment and suppressed iodide-related defect states in the perovskite film derived from the moderately aged precursor.

Then, top-view and cross-sectional SEM were employed to further elucidate the influence of precursor aging duration on the morphological evolution of the resulting perovskite films [Figure 3D and E, Supplementary Figure 11]. The fresh perovskite film exhibited relatively small and irregularly packed grains, accompanied by noticeable grain boundaries and localized residual $PbI_2$ domains. By contrast, the moderately aged film displayed considerably enlarged grains with improved lateral connectivity and a compact microstructure.

Cross-sectional SEM images revealed that the moderately aged sample comprised vertically continuous grains spanning the entire film thickness, whereas the fresh sample showed a stacked grain structure with frequent grain boundaries [Supplementary Figure 11C and D]. This evolution of perovskite grains indicates that moderate aging promoted the crystal growth throughout the film thickness rather than merely affecting surface morphology. The reduced residual $PbI_2$ in the moderately aged sample suggests more complete perovskite conversion and uniform grain growth.

The morphological differences were further corroborated by atomic force microscopy [Figure 3F and G]. The RMS roughness of the perovskite film decreased from 27.2 nm for the fresh sample to 22.4 nm for the moderately aged sample, indicating a smoother and more uniform surface. This reduced surface roughness reflects suppressed heterogeneous nucleation and more homogeneous crystal growth, which is consistent with the enhanced crystallinity revealed by XRD analysis.

The improvement in the film structural quality was reflected in its photophysical properties. As depicted in Figure 3H, the steady-state PL spectrum of the moderately aged sample exhibited a markedly enhanced emission intensity compared to that of the fresh sample. The photoluminescence quantum yield (PLQY) increased from 0.14% for the fresh sample to 1.04% for the moderately aged sample, while the corresponding quasi-Fermi level splitting (QFLS) increased from 1.129 to 1.184 eV [Supplementary Figure 12]. These improvements indicate enhanced radiative recombination efficiency and reduced nonradiative recombination losses. This trend was further confirmed by time-resolved photoluminescence (TRPL) measurements [Figure 3I], with the carrier lifetime increasing from 682.83 ns for the fresh sample to 947.41 ns for the moderately aged one. The prolonged carrier lifetime directly reflects reduced trap-assisted recombination and improved charge carrier dynamics in the perovskite film derived from the moderately aged precursor.

The PSCs featuring an ITO/$SnO_2$/perovskite/PEAI/Spiro-OMeTAD/Ag architecture were fabricated to assess the influence of moderate aging on the photovoltaic performance. All layers were deposited in ambient air, except the Ag electrode, which was deposited by high-vacuum evaporation. Figure 4A shows the *J-V* curves and corresponding champion photovoltaic parameters of fresh and moderately aged devices. The fresh device achieved a PCE of 23.05% with an open-circuit voltage ($V_{OC}$) of 1.128 V, short-circuit current density ($J_{SC}$) of 25.65 mA $cm^{-2}$, and fill factor (FF) of 79.5%. In contrast, the champion device derived from the moderately aged solution yielded a higher PCE of 24.52%, with a $V_{OC}$ of 1.145 V, $J_{SC}$ of 26.12 mA $cm^{-2}$, and FF of 81.94%. As shown in Supplementary Table 4, the HI of fresh and moderately aged PSCs are calculated as 2.91% and 1.84%, respectively. To evaluate the reproducibility and consistency of device performance, we examined the statistical distributions of key photovoltaic parameters [Supplementary Figure 13]. The corresponding means and standard deviations are summarized in Supplementary Table 5. PSCs prepared from the moderately aged precursor exhibited higher and more concentrated photovoltaic parameter distributions than their fresh counterparts, which reflected the robust reproducibility of the enhanced performance. The improved $J_{SC}$ and FF were primarily attributed to the enhanced crystallinity and reduced defect density within the perovskite bulk, while the improvement in $V_{OC}$ was mainly linked to the suppressed nonradiative recombination, as evidenced by the prolonged carrier lifetimes revealed by PL spectroscopy. The elevation in $J_{SC}$ is further corroborated by the EQE spectra shown in Figure 4B, which reveal that the moderately aged device displayed superior photon-to-electron conversion efficiencies across the measured range. The most pronounced enhancement occurred in the short-wavelength region (300-400 nm), suggesting more efficient charge-carrier collection and reduced recombination losses near the illuminated side of the device. Consequently, the integrated $J_{SC}$ increased from 23.04 mA $cm^{-2}$ for the fresh device to 23.98 mA $cm^{-2}$ for the moderately aged one. This spectral improvement is consistent with the through-out grain structure observed in the SEM images, which effectively facilitates efficient longitudinal charge collection.

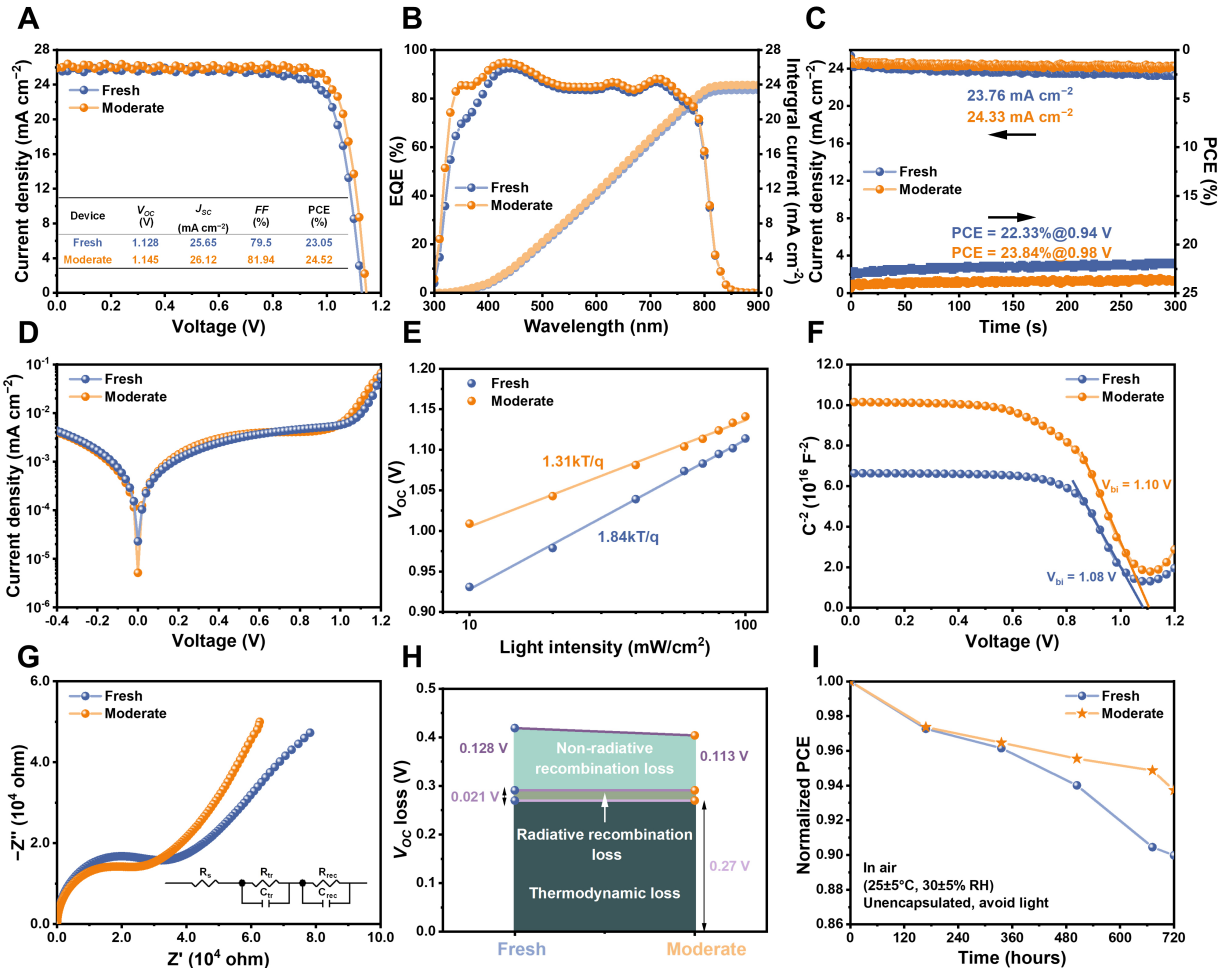



**Figure 4.** Photovoltaic performance and characteristics of PSCs. (A) The *J-V* curves of the champion devices based on the fresh and moderate solutions; (B) the EQE spectra and the integrated current density of the fresh and moderately aged devices; (C) steady-state output of the devices at maximum power point; (D) the dark *J-V* curves of the fresh and moderately aged devices; (E) dependence of $V_{OC}$ on light intensity for the fresh and moderately aged devices; (F) Mott-Schottky curves for the fresh and moderately aged devices; (G) EIS curves for the fresh and moderately aged devices; (H) analysis of the $V_{OC}$ loss for the fresh and moderately aged devices; (I) PCE decay of the best-performing fresh and moderately aged devices stored in ambient conditions (RH = 25%-35%) without encapsulation. PSCs: Perovskite solar cells; EQE: external quantum efficiency; EIS: electrochemical impedance spectroscopy; PCE: power conversion efficiency; RH: relative humidity; FF: fill factor; $R_s$: series resistance; $R_{tr}$: transport resistance; $R_{rec}$: recombination resistance; $C_{tr}$: transport capacitance; $C_{rec}$: recombination capacitance; *J-V*: current density-voltage; $V_{OC}$: open-circuit voltage; $J_{SC}$: short-circuit current density.

Figure 4C shows the SPO of the devices monitored under the bias at the maximum power point, with operating voltages of 0.94 and 0.98 V used for the fresh and moderately aged devices, respectively. During 300 s of continuous SPO measurement, the moderately aged device exhibited a higher and more stable steady-state current density of 24.33 mA cm$^{-2}$, compared with 23.76 mA cm$^{-2}$ for the fresh device. Correspondingly, the moderately aged device delivers an improved steady-state PCE of 23.84%, exceeding that of the fresh device at 22.33%. The improved short-term steady-state power output of the moderately aged device may be associated with the reduced amount of residual $PbI_2$ at grain boundaries, leading to more efficient and stable charge extraction. Figure 4D presents the dark *J-V* curves of the moderately aged and fresh PSCs, with the corresponding dark saturation current densities ($J_0$) equaling 5.15 × 10$^{-6}$ mA cm$^{-2}$ and 2.29 × 10$^{-5}$ mA cm$^{-2}$, respectively. This pronounced reduction in $J_0$ indicates suppressed leakage current and nonradiative recombination in the moderately aged device, consistent with the enhanced crystallinity and more complete $PbI_2$ conversion achieved through moderate precursor aging.

The dependence of $V_{OC}$ and $J_{SC}$ on incident light intensity was further examined to elucidate the charge separation and recombination kinetics in the PSCs. Measurements were carried out under illumination intensities ranging from 100 mW cm$^{-2}$ (1 Sun) to 10 mW cm$^{-2}$ (0.1 Sun). The $V_{OC}$ can be described by the following Equation (1):

$$V_{OC} = nkTq^{-1} \ln\left(\frac{J_{SC}}{J_0} + 1\right) \quad (1)$$

where $n$ is the ideality factor, $k$ is the Boltzmann constant, $T$ is the temperature, $q$ is the elementary charge, and $J_0$ denotes the dark saturation current density. Under illumination, $J_{SC}$ is much larger than $J_0$ and increases with light intensity ($I$) following a power-law relationship $J_{SC} \propto I^{\alpha}$, where $\alpha$ is the corresponding exponent. Accordingly, $V_{OC}$ varies linearly with the natural logarithm of light intensity, and the slope of this linear relationship is proportional to n. As illustrated in Figure 4E, the moderately aged device yielded a reduced slope of 1.31 $kTq^{-1}$ compared to the 1.84 $kTq^{-1}$ of the fresh device, which indicates that the moderate precursor aging effectively suppressed trap-assisted recombination, consistent with the improved $V_{OC}$. Regarding the dependence of $J_{SC}$ on illumination intensity [Supplementary Figure 14], both devices exhibited a near-linear scaling behavior. The fresh device yields an $\alpha$ value of 0.982, while the moderately aged device shows a higher $\alpha$ of 1.007. The $\alpha$ value closer to 1 indicates more efficient charge collection and reduced bimolecular recombination losses in the moderately aged device. SCLC measurements were performed to evaluate the electron- and hole-related trap-state density ($N_{trap}$) in perovskite films, respectively. Supplementary Figure 15 shows that the trap-filled limit voltages ($V_{TFL}$) of the fresh and moderately aged electron-only devices were 0.32 V and 0.18 V, respectively, while those of the corresponding hole-only devices were 0.84 V for fresh and 0.71 V for the moderately aged sample. The $N_{trap}$ was calculated according to Equation (2):

$$N_{trap} = \frac{2\varepsilon_r \varepsilon_0 V_{TFL}}{qL^2} \quad (2)$$

where $\varepsilon_r$ is the relative dielectric constant of the perovskite (46.9, as reported previously[42]), $\varepsilon_0$ is the vacuum permittivity, $q$ is the elementary charge, and $L$ is the thickness of the perovskite layers (644 nm for the fresh and 682 nm for the moderately aged perovskite films). Accordingly, the electron-related $N_{trap}$ values of the fresh and moderately aged perovskite films were determined as 4.00 × 10$^{15}$ cm$^{-3}$ and 2.01 × 10$^{15}$ cm$^{-3}$, respectively, whereas the corresponding hole-related trap-state densities were calculated to be 1.05 × 10$^{16}$ cm$^{-3}$ for the fresh sample and 7.91 × 10$^{15}$ cm$^{-3}$ for the moderately aged sample. These results indicate that moderate precursor aging reduced both electron- and hole-related trap-state densities in the perovskite films. The reduced trap-state densities may have facilitated carrier transport and suppressed trap-related nonradiative recombination, consistent with the lower dark saturation current observed in the moderately aged devices.

Mott-Schottky analysis [Figure 4F] revealed an increase in the built-in potential ($V_{bi}$) from 1.08 V in the fresh device to 1.10 V in the moderately aged device, suggesting a strengthened internal electric field favoring efficient charge separation and transport after moderate aging. To gain further insights into interfacial processes and impedance responses under operating conditions, EIS measurements were conducted. As shown in Figure 4G, the moderately aged device exhibited a smaller semicircle in the high-frequency region, which suggests reduced resistive losses associated with charge transfer. In the low-frequency region, a more pronounced linear tail is observed for the moderately aged device, corresponding to an increased boundary impedance (ZB), which implies restrained ion accumulation at the interfaces. These impedance characteristics collectively account for the improved FF and enhanced operational stability. Additionally, we quantitatively analyzed $V_{OC}$ loss, distinguishing contributions from thermal radiation, radiative recombination, and nonradiative recombination. As shown in Figure 4H, non-radiative recombination accounted for 0.128 V in the fresh device and 0.113 V in the moderately aged device, which explains the decreased $V_{OC}$ loss.

Finally, the long-term storage stability of unencapsulated PSCs was tested under 25 ± 5 °C and 30% ± 5% RH [Figure 4I]. The moderately aged device demonstrated improved storage stability, retaining over 93% of its initial PCE after 720 h, whereas the PCE of the fresh device degraded to < 90% under the same conditions.

## CONCLUSIONS

The early-stage aging of $PbI_2$ precursor solutions plays a pivotal role in their coordination chemistry and the structural evolution of two-step perovskite solar cells fabricated under ambient conditions. In the identified moderate-aging window, progressive iodide incorporation into the $Pb^{2+}$ coordination shell refines nanoscale iodoplumbate species, enabling the formation of compact and highly oriented (00n)-dominated $PbI_2$ templates. This optimized precursor state facilitates the complete conversion of $PbI_2$ to perovskite, formation of enlarged and continuous perovskite grains, defect density reduction, and nonradiative recombination suppression, ultimately enhancing device performance. These findings establish precursor aging as an effective chemical strategy linking solution-state coordination equilibrium with device performance and provide a simple and scalable approach to achieving high-efficiency, reproducible perovskite solar cells via ambient processing.

## DECLARATIONS

### Authors' contributions

Methodology, formal analysis, and writing of the manuscript: Zhang, M.
Assisted with experiments and characterization: Liao, X.; Mi, K.; Li, L.; Yang, W.
Supervision, project administration, and funding acquisition: Zeng, Q.; Liu, F.

### Availability of data and materials

Some data are presented in the "Supplementary Materials" section. Other raw data that support the findings of this study are available from the corresponding author upon reasonable request.

### AI and AI-assisted tools statement

Not applicable.

### Financial support and sponsorship

This work was supported by the National Natural Science Foundation of China (52525405, 52604562) and the Major Scientific and Technological Project of Changsha (kq2501002).

### Conflicts of interest

All authors declared that there are no conflicts of interest.

### Ethical approval and consent to participate

Not applicable.

### Consent for publication

Not applicable.

### Copyright

© The Author(s) 2026.

### Supplementary Materials

Supplementary Materials

## REFERENCES

1. Chen, P.; Xiao, Y.; Li, S.; et al. The promise and challenges of inverted perovskite solar cells. *Chem. Rev.* **2024**, *124*, 10623-700. DOI
2. Jiang, Q.; Zhu, K. Rapid advances enabling high-performance inverted perovskite solar cells. *Nat. Rev. Mater.* **2024**, *9*, 399-419. DOI

3. Tian, Y.; Zhang, X.; Zhao, K.; et al. High-entropy hybrid perovskites with disordered organic moieties for perovskite solar cells. *Nat. Photon.* **2024**, *18*, 960-6. DOI
4. Liu, Z.; Lin, R.; Wei, M.; et al. All-perovskite tandem solar cells achieving >29% efficiency with improved (100) orientation in wide-bandgap perovskites. *Nat. Mater.* **2025**, *24*, 252-9. DOI
5. Xiong, Z.; Zhang, Q.; Cai, K.; et al. Homogenized chlorine distribution for >27% power conversion efficiency in perovskite solar cells. *Science* **2025**, *390*, 638-42. DOI
6. Luo, S.; Liu, D.; Deng, X.; et al. Boron-halide interactions for crystallization regulation of a 1.68 eV wide-bandgap perovskite prepared *via* a two-step method. *Energy. Environ. Sci.* **2025**, *18*, 10364-79. DOI
7. Yu, Z.; Ma, J.; Yang, X.; et al. Levetiracetam-assisted perovskite crystallization and tripartite lead iodide reduction in perovskite solar cells. *Adv. Mater.* **2026**, *38*, e12171. DOI
8. Chen, M.; Qin, Z.; Zhang, Z.; et al. Low-temperature sequential deposition for efficient inverted perovskite solar cells. *Nat. Commun.* **2025**, *16*, 5746. DOI PubMed PMC
9. Zeng, Q.; Xiao, H.; Ma, Q.; et al. Highly layer-oriented $PbI_2$ films enabling all-air processed perovskite solar cells. *Adv. Energy. Mater.* **2024**, *14*, 2401279. DOI
10. He, J.; Sheng, W.; Liu, K.; et al. Unraveling the reaction dynamics mechanism and thermodynamic pathway of lead iodide and organic cations in the two-step sequential deposition process. *Energy. Environ. Sci.* **2025**, *18*, 6983-7004. DOI
11. Wang, J.; Yuan, L.; Luo, H.; et al. Ambient air processed highly oriented perovskite solar cells with efficiency exceeding 23% via amorphous intermediate. *Chem. Eng. J.* **2022**, *446*, 136968. DOI
12. Zhang, J.; Wu, J.; Barabash, A.; et al. Precise control of process parameters for >23% efficiency perovskite solar cells in ambient air using an automated device acceleration platform. *Energy. Environ. Sci.* **2024**, *17*, 5490-9. DOI
13. He, J.; Sheng, W.; Yang, J.; et al. Omnidirectional diffusion of organic amine salts assisted by ordered arrays in porous lead iodide for two-step deposited large-area perovskite solar cells. *Energy. Environ. Sci.* **2023**, *16*, 629-40. DOI
14. Xia, Y.; Zhu, M.; Qin, L. Organic-inorganic hybrid quasi-2D perovskites incorporated with fluorinated additives for efficient and stable four-terminal tandem solar cells. *Energy. Mater.* **2023**, *3*, 300004. DOI
15. Duan, H.; Jin, J.; Liu, X.; et al. Electron-donor/-acceptor ratio-guided molecular engineering for buried interface optimization in n-i-p perovskite solar cells. *Energy. Mater.* **2026**, *6*, 600031. DOI
16. Zhou, B.; Zhao, P.; Guo, J.; et al. Solvent-additive cascade engineering enables single-oriented perovskite films with facet-driven performance and stability. *Energy. Environ. Sci.* **2025**, *18*, 9865-76. DOI
17. Zhang, Y.; Yang, T.; Lee, S.; Liu, S.; Zhao, K.; Park, N. Stabilizing α-phase $FAPbI_3$ perovskite induced by an ordered solvated quasi-crystalline $PbI_2$. *ACS. Energy. Lett.* **2024**, *9*, 159-67. DOI
18. Yu, X.; Fang, Z.; Lin, S.; et al. Polyvinyl pyrrolidone induced “confinement effect” on $PbI_2$ and the improvement on crystallization and thermal stability of perovskite. *Small* **2024**, *20*, 2306101. DOI
19. Du, Z.; Ma, Z.; Yu, T.; et al. $PbI_2$ intercalation and residual elimination strategy for sequential inverted perovskite solar cells. *Chem. Eng. J.* **2025**, *503*, 158587. DOI
20. McMeekin, D. P.; Wang, Z.; Rehman, W.; et al. Crystallization kinetics and morphology control of formamidinium-cesium mixed-cation lead mixed-halide perovskite via tunability of the colloidal precursor solution. *Adv. Mater.* **2017**, *29*, 1607039. DOI
21. Xie, Y.; Xu, X.; Cui, Y.; et al. Colloidal chemistry of $MAPbI_3$ perovskite ink using 2-methoxyethanol as the solvent. *Colloids. Surf. A. Physicochem. Eng. Asp.* **2023**, *677*, 132406. DOI
22. Wang, K.; Duan, Z.; Liu, H.; et al. Stabilizing precursor solutions by proton-rich additive for high-performance air-processed solar cells. *Small* **2025**, *21*, e2501184. DOI
23. Liu, Y.; Wang, J.; Liu, T.; et al. Stabilized perovskite ink for scalable coating enables high-efficiency perovskite modules. *Sci. Adv.* **2026**, *12*, eaec0915. DOI PubMed PMC
24. Zhang, Y.; Xing, Z.; Fan, B.; et al. Uncovering aging chemistry of perovskite precursor solutions and anti-aging mechanism of additives. *Angew. Chem. Int. Ed.* **2023**, *62*, e202215799. DOI
25. Hu, S.; Hou, P.; Dou, Y.; et al. Precursor stabilization strategies via vapor-solid reaction for reproducible and high-efficiency vapor-deposited perovskite solar cells. *ACS. Nano.* **2026**, *20*, 5007-20. DOI
26. Wu, N.; Yang, T.; Wang, Z.; et al. Stabilizing precursor solution and controlling crystallization kinetics simultaneously for high-performance perovskite solar cells. *Adv. Mater.* **2023**, *35*, e2304809. DOI
27. Hu, W.; Yang, J.; Yang, C.; et al. Stabilizing perovskite precursors with the reductive natural amino acid for printable mesoscopic perovskite solar cells. *J. Energy. Chem.* **2024**, *90*, 32-9. DOI
28. Li, L.; Zeng, Q.; Liao, X.; et al. D-isoascorbic acid endows formamidinium iodide with robust storage stability and wide-bandgap perovskite with reduced phase segregation. *Adv. Funct. Mater.* **2026**, *36*, e75247. DOI

29. Ye, J.; Sheng, W.; He, J.; et al. Extending shelf-life of two-step method precursor solutions through targeted regulation for highly efficient and reproducible perovskite solar cells. *Angew. Chem. Int. Ed.* **2024**, *63*, e202411708. DOI
30. Yan, K.; Long, M.; Zhang, T.; et al. Hybrid halide perovskite solar cell precursors: colloidal chemistry and coordination engineering behind device processing for high efficiency. *J. Am. Chem. Soc.* **2015**, *137*, 4460-8. DOI
31. Flatken, M. A.; Hoell, A.; Wendt, R.; et al. Small-angle scattering to reveal the colloidal nature of halide perovskite precursor solutions. *J. Mater. Chem. A.* **2021**, *9*, 13477-82. DOI
32. O'Kane, M. E.; Smith, J. A.; Kilbride, R. C.; et al. Exploring nanoscale structure in perovskite precursor solutions using neutron and light scattering. *Chem. Mater.* **2022**, *34*, 7232-41. DOI PubMed PMC
33. Radicchi, E.; Mosconi, E.; Elisei, F.; Nunzi, F.; De Angelis, F. Understanding the solution chemistry of lead halide perovskites precursors. *ACS. Appl. Energy. Mater.* **2019**, *2*, 3400-9. DOI
34. Shargaieva, O.; Kuske, L.; Rappich, J.; Unger, E.; Nickel, N. H. Building blocks of hybrid perovskites: a photoluminescence study of lead-iodide solution species. *ChemPhysChem* **2020**, *21*, 2327-33. DOI PubMed PMC
35. Intan, N. N.; Sorenson, B. A.; Choi, Y. K.; et al. Smaller is better: the case for lower-order iodoplumbate species dominating $MAPbI_3$/dimethylformamide solutions. *Chem. Mater.* **2024**, *36*, 8424-36. DOI
36. Shin, G. S.; Kim, S.; Zhang, Y.; Park, N. A correlation between iodoplumbate and photovoltaic performance of perovskite solar cells observed by precursor solution aging. *Small. Methods.* **2020**, *4*, 1900398. DOI
37. Lee, S.; Lim, S. Y.; Kim, T.; et al. High-valent iodoplumbate-rich perovskite precursor solution via solar illumination for reproducible power conversion efficiency. *J. Phys. Chem. Lett.* **2021**, *12*, 1676-82. DOI
38. Naikaew, A.; Krajangsang, T.; Srathongsian, L.; et al. Photoexcitation of perovskite precursor solution to induce high-valent iodoplumbate species for wide bandgap perovskite solar cells with enhanced photocurrent. *Sci. Rep.* **2023**, *13*, 6125. DOI PubMed PMC
39. Popov, G.; Mattinen, M.; Hatanpää, T.; et al. Atomic layer deposition of $PbI_2$ thin films. *Chem. Mater.* **2019**, *31*, 1101-9. DOI
40. Wang, F.; Wang, T.; Sun, Y.; et al. Two-step perovskite solar cells with > 25% efficiency: unveiling the hidden bottom surface of perovskite layer. *Adv. Mater.* **2024**, *36*, e2401476. DOI
41. Shao, W.; Wang, H.; Ye, F.; et al. Modulation of nucleation and crystallization in $PbI_2$ films promoting preferential perovskite orientation growth for efficient solar cells. *Energy. Environ. Sci.* **2023**, *16*, 252-64. DOI
42. Han, Q.; Bae, S. H.; Sun, P.; et al. Single crystal formamidinium lead iodide ($FAPbI_3$): insight into the structural, optical, and electrical properties. *Adv. Mater.* **2016**, *28*, 2253-8. DOI


**Disclaimer/Publisher's Note:** All statements, opinions, and data contained in this publication are solely those of the individual author(s) and contributor(s) and do not necessarily reflect those of OAE and/or the editor(s). OAE and/or the editor(s) disclaim any responsibility for harm to persons or property resulting from the use of any ideas, methods, instructions, or products mentioned in the content.



© The Author(s) 2026. Open Access This article is licensed under a Creative Commons Attribution 4.0 International License (https://creativecommons.org/licenses/by/4.0/), which permits unrestricted use, sharing, adaptation, distribution and reproduction in any medium or format, for any purpose, even commercially, as long as you give appropriate credit to the original author(s) and the source, provide a link to the Creative Commons license, and indicate if changes were made.